Validating Reactive Transport Models of CO2-brine-Rock Reactions in Caprocks Using Observations from a Natural CO2 Reservoir

Available online at www.sciencedirect.com

ScienceDirect

Energy Procedia 114 (2017) 4902 – 4916

Energy Procedia

13th International Conference on Greenhouse Gas Control Technologies, GHGT-13, 14-18 November 2016, Lausanne, Switzerland

Validating reactive transport models of CO_2-brine-rock reactions in caprocks using observations from a natural CO_2 reservoir

Niko Kampman[a,*], Pieter Bertier[b], Andreas Busch[a], Jeroen Snippe[a], Jon Harrington[c], Vitaliy Pipich[d], Alex Maskell[e] and Mike Bickle[e]

[a]*Shell Global Solutions International BV, Kessler Park 1, 2288 GS Rijswijk, The Netherlands*
[b]*RWTH Aachen University, Clay and Interface Mineralogy, Bunsenstrasse 8, 52072 Aachen, Germany*
[c]*British Geological Survey, Environmental Science Centre, Keyworth, Nottingham NG12 5GG, UK*
[d]*Jülich Centre for Neutron Science (JCNS), Heinz Maier-Leibnitz Zentrum (MLZ),1 Lichtenbergstraße, 85747 Garching, Germany*
[e]*Department of Earth Sciences, University of Cambridge, Downing Street, Cambridge CB2 3EQ, UK*

Abstract

Storage of anthropogenic CO_2 in geological formations relies on impermeable caprocks as the primary seal preventing buoyant super-critical CO_2 escaping. Although natural CO_2 reservoirs demonstrate that CO_2 may be stored safely for millions of years, uncertainty remains in predicting how caprocks will react with acid CO_2-bearing brines. This uncertainty poses a challenge to the assessment of carbon capture and storage schemes. Prediction of caprock behaviour is based primarily on theoretical modelling and laboratory experiments. However, the reactive transport phenomena cannot be reproduced in laboratory experiments over sufficient timescales, theoretical models need calibration against observational data and existing studies on natural caprocks have not resolved mineral reactions. Here we report a detailed description of a stacked sequence of CO_2 reservoir-caprock systems exposed to CO_2-rich fluids over ~ 10^5 years, a time-scale comparable with that needed for effective geological carbon storage. Fluid-mineral reactions in the base of multiple caprocks is driven by diffusion of CO_2 and minor H2S from the underlying reservoirs. The reactions include dissolution of hematite, dolomite and K-feldspar and precipitation of Fe-bearing dolomite, gypsum, pyrite and illite over centimetre length-scales. The mineral dissolution reactions generate transient increases in porosity, as determined by neutron scattering measurements, but the propagation of mineral reaction fronts is retarded by the reaction stoichiometry and mineral precipitation. Modelling of the mineral reaction fronts shows that the alteration is sluggish, developing over a >10^4 year period. The results attest to the significance of transport-limited reactions to the long-term integrity of sealing behaviour in caprocks exposed to CO_2.

* Corresponding author. *E-mail address:* niko.kampman@shell.com

Peer-review under responsibility of the organizing committee of GHGT-13.
doi:10.1016/j.egypro.2017.03.1632

Peer-review under responsibility of the organizing committee of GHGT-13.

Keywords:

1. Introduction

Carbon capture and storage is essential to managing society's transition to low-CO_2 energy sources [1, 2]. The CO_2 will be injected into geological formations where storage will rely on the buoyant CO_2 being trapped under impermeable caprocks. CO_2 dissolves in water to form a weak acid and one concern is that the acidified brines will corrode caprocks. Laboratory and modelling studies predicting caprock behaviour need verification in natural systems over appropriate timescales. We describe two caprocks to a stacked sequence of natural CO_2-saturated reservoirs where the mineral reaction fronts have only penetrated 7-8 cm into the caprocks in ~ 10^4 to 10^5 years. The migration of the CO_2 is effectively retarded by the high tortuosity of the pore network and the progress of the mineral-fluid reactions is further delayed by the reaction stoichiometry and mineral saturation in the pore fluid.

The caprocks in sedimentary successions suitable for CO_2 storage will most commonly comprise mudstones or shales and these act as barriers to CO_2 migration by two mechanisms [3]. Their low permeabilities ($<10^{-19}$ m^2) restrict fluid fluxes to very low rates. Further capillary entry pressures for CO_2 of 0.5 to 5 MPa [4] will restrict penetration of CO_2, allowing transport of CO_2 only by sluggish diffusion in the brine phase. However, the addition of CO_2 forms acid brines which react with caprocks to drive both dissolution and precipitation of minerals [3, 5, 6]. Of particular concern is that the CO_2-rich brines may penetrate more permeable pathways and fractures and that the mineral dissolution reactions will enhance the penetration of the CO_2. A fundamental difficulty in the prediction of such reactive transport is that the nature and kinetics of the mineral dissolution and precipitation reactions in natural settings are poorly constrained [7]. How permeability/diffusivity will be changed will depend on the balance between the rates of dissolution and precipitation and the consequent changes in porosity and pore structure. It is predicted that the initial dissolution of more rapidly reacting carbonate and oxy-hydroxide phases will buffer the pH of CO_2-saturated brines to ~5 followed by the more sluggish reactions with the silicate phases which further increase pH and cause re-precipitation of carbonate minerals [5, 6, 8]. The modelling of these interdependent dissolution/precipitation reactions is hindered by uncertainties related to the kinetic rate constants, complex mineralogies, mineral surface areas, and changes in porosity and permeability [7].

We address this fundamental gap in our knowledge of the long-term impacts of CO_2-charged fluids on caprock integrity by examining caprock recovered from a natural CO_2 reservoir. Although this reservoir is at much shallower depths and lower pressures than needed for geological carbon storage, the reactions studied here between minerals and CO_2-saturated brines are little affected by pressure. Mineralogical and petrophysical measurements are used to assess the impacts of CO_2 promoted reactions and this data is used to constrain analytical and numerical reaction-diffusion models, elucidating the time-scales of alteration.

Core and fluid samples were collected from a sequence of CO_2-charged reservoirs and their intervening caprocks during scientific drilling, within the footwall of the Little Grand Wash Fault, Green River, Utah [9] (Fig 1). The 325m drillhole transected reservoirs of CO_2-charged brine in the Middle Jurassic Entrada and Lower Jurassic Navajo Sandstone, and the intervening Middle Jurassic Carmel Formation caprock. The geochemistry of fluid samples collected at formation pressures through the Navajo Sandstone reservoir, tracks contemporary filling via artesian flow of CO_2 and CO_2-saturated brines through the faults [10]. The reservoir fluids are mixtures of Na-Cl-SO4 brine and meteoric groundwater with low pH (5.1 to 5.3), reducing (0 to -50mV), SO4-rich and contain trace quantities of H_2S and CH_4. The migrating CO_2 and CO_2-saturated brine originates from a supercritical accumulation of CO_2 within Carboniferous strata at depth. U-Th geochronology of carbonate veining in associated faults attests to CO_2 out-gassing regionally for circa 400 ka and locally for at least 114 ka [11]. Geochemical cycles in vein chemistry are attributed to cyclic charging of the reservoir following periods of crustal unloading during regional deglaciations [12].

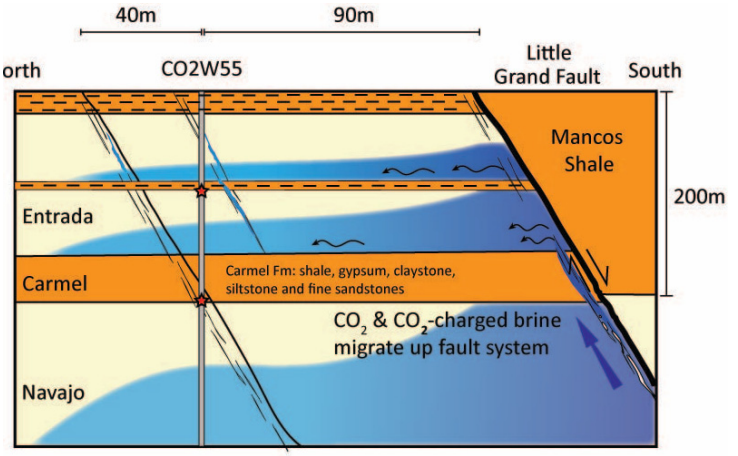

Figure 1 Schematic cross section of the stratigraphy penetrated by the CO2W55 drillhole, Green River, Utah. Red stars indicate the location of core samples used in this study

2. Method

Details of the drilling and downhole fluid sampling of well CO2W55 are presented in [11] and [12]. Further details of sampling and analysis of the Carmel Formation caprock are presented in the methodologies applied in this paper are presented in [13].

2.1. Drill core sampling

HQ core (63.5 mm diameter) samples of the caprock intervals, recovered from well CO2W55 near the town of Green River, Utah, were slabbed, and then sliced parallel to bedding at ~3-5mm resolution, using a steel blade rock saw. Whole core samples were collected from the contact between the base of the Carmel Formation and Navajo Sandstone, and from the contact between the Entrada Sandstone and an inter-reservoir seal (red stars: Figure 1).

Approximately 2-5g of air dried sample was powdered to ⩽100 μm size in a ball mill using an agate container and balls, and subsamples were taken for individual analyses. Samples for X-ray diffraction measurements were crushed and milled separately.

2.2. XRD measurements

XRD measurements to determine mineralogy have been performed at RWTH Aachen University as stated in ref. [15], except the counting time is 20 s for each step of 0.02° 2θ recorded from 2° to 92° 2θ. Rock samples are crushed manually in a mortar with care taken to avoid strain damage and crushed material together with an internal standard (Corundum, 20 wt. %) is milled in ethanol with a McCrone Micronising mill (15 min). Quantitative phase analysis is performed by Rietveld refinement using BGMN software, with customized clay mineral structure models [16]. The precision of these measurements, from repetitions, is better than 0.1 wt% for phases of which the content is above 2%. The accuracy cannot be determined because of the lack of pure clay mineral standards, but is estimated to be better than 10% (relative).

2.3. Stable isotopes

Carbonate mineral $\delta^{13}C$ and $\delta^{18}O$ were determined at the University of Cambridge on duplicate subsamples of 300–500 μg using a Thermo Gas Bench attached to a Thermo MAT 253 mass spectrometer in continuous flow mode, with an analytical precision of ±0.12‰ and ±0.20‰, respectively, (2σ). $\delta^{13}C$ and $\delta^{18}O$ results are reported, relative to the VPDP and VSMOW standards, as averages of these duplicate analyses, with error bars that are the 2σ s.e. of duplicate averages.

2.4. Scanning electron microscopy and electron microprobe analyses

Back-scatter electron and secondary electron images were obtained using the JEOL 820 scanning electron microscope in the Department of Earth Sciences, University of Cambridge, with an accelerating voltage of 20 kV and 1 nA beam current. Electron microprobe analyses of mineral compositions were determined using a Cameca SX-100 electron microprobe at the University of Cambridge (15 kV, 10 nA; beam diameter 5 μm) with fayalite, rutile, corundum, periclase and pure Co, Ni, Mn, Cr, Zn and Cu standards.

2.5. Small angle neutron scattering

Sample porosity, specific surface area and the pore surface and pore volume fractal dimensions were analysed using SANS and VSANS techniques. Experiments were carried out using the instrument KWS-1 (SANS) and KWS-3 (VSANS) operated by the Jülich Center for Neutron Science at Heinz-Meier-Leibnitz Zentrum in Garching, Germany. Carmel caprock samples were cut parallel to bedding, fixed on quartz glass and polished to a thickness of 200 μm for measurements. Samples were dried at room temperature and measurements performed under ambient pressure and temperature conditions. The target area on the sample was defined by a cadmium mask with an 8 mm diameter window.

For (V)SANS measurements, a collimated neutron beam is elastically scattered by the sample and position-sensitive detectors measure the scattering intensity I(Q) as a function of the scattering angle, θ. The momentum transfer Q (nm^{-1}) is related to the scattering angle θ by $Q = (4\pi/\lambda)\sin(\theta/2)$, where λ is the wavelength of the neutrons. Thus, the size range of features accessible with neutron scattering depends on the neutron wavelength λ and the range in the scattering angle θ. SANS data at KWS-1 were collected at wavelengths of λ = 0.69 nm with a wavelength distribution of the velocity selector $\Delta\lambda/\lambda = 0.10$ (full width at half-maximum). Measurements were performed at sample-to-detector distances of 19.7, 7.7 and 1.7 m, covering a wide Q-range of 0.02–2.6 nm^{-1}. VSANS data at KWS-3 were collected at λ = 1.28 nm, $\Delta\lambda/\lambda = 0.2$ and a sample-to-detector distance of 9.5 m, covering a Q-range from 0.024 to 0.0016, nm^{-1}. Hence, pore radii for the combined SANS and VSANS measurements range between 1 nm and 1.5 μm ($r \approx 2.5/Q$). Instrument data analysis and background subtraction was carried out using the QtiKWS software provided by the Jülich Center for Neutron Science. During background subtraction, the lower pore sizes were cut off at 12 Å, to remove artefacts arising from Bragg scattering from ordered stacking of clay minerals. For the combined SANS and VSANS measurements, this results in scattering intensity I(Q) (nm^{-1}) versus the momentum transfer, Q (nm^{-1}) relationships.

Pore volume distributions *f(r)* as a function of length scale, *r*, porosity, ϕ, and specific surface area, SSA, were calculated from the (V)SANS data following Porod's Law, using the PRINSAS software [17]. The integral of the scattered intensity in reciprocal space in a two-phase system is the Porod invariant Qinv from which the porosity ϕ is obtained directly

$$Q_{inv} = \int_0^\infty Q^2 I(Q)\, dQ = 2\pi^2(\Delta p^*)^2\phi(1-\phi) \quad (1)$$

We assumed that the scattering intensity of pore features is directly proportional to the scattering contrast between matrix and pore

$$I(Q) = \phi V_p (p_1^* - p_2^*)^2 P(Q) S(Q) \quad (2)$$

Here, p_1^* and p_2^* are the coherent scattering length densities (SLDs) for neutrons for the two phases, shale matrix and air (pore), respectively. The terms *P(Q)* and *S(Q)* denote the form and structure factors, for which analytical expressions exist for different geometries of scatterers, including mass and surface fractals [18]. The terms ϕ and V_p are the volume fraction of the dispersed phase and the volume per scatterer, respectively. The SLD Δp^* of each mineral was calculated as

$$\Delta p^* = \frac{N_A b_i}{M_i} d_i \tag{3}$$

where b_i and M_i are scattering length and atomic mass of the i^{th} element in the mineral, d_i is the mass density of the i^{th} mineral and N_A is the Avogadro number. Scattering length densities were calculated using the U.S. National Institute of Science and technology (NSIT) SLD calculator (http://www.ncnr.nist.gov/resources/activation/). As the scattering contrast between the shale matrix and the pores is large, all scattering is attributed to nano-pore features. SLD values for the shale matrix studied range between 3.2 and 3.4 × 10^{-14} m^{-2}; for air, it can be considered to be zero.

The specific surface area, SSA, of surface fractals scales with the length scale *r* as [18, 19]:

$$SSA = \frac{\lim_{Q\to\infty}\left[Q^{6-D_S} I(Q)\right]}{\pi(\Delta p^*)^2 \rho F(D_S)} r^{2-D_S} \tag{4}$$

Where Δp^* is the scattering length density contrast, ρ is mass density, D_s is the surface fractal dimension and

$$F(D_s) = \Gamma(5 - D_s) sin\left[(3 - D_s)\left(\frac{\pi}{2}\right)\right]/(3 - D_s) \tag{5}$$

Experimentally determined I(Q) curves are modelled, after background subtraction, using the polydisperse hard sphere model implemented in the software code PRINSAS.

Effective diffusion values D_e (m^2 s^{-1}) of the samples were calculated from the fractal dimensions of the pore and grain surface derived from the (V)SANS data. Typically, the effective diffusivity of a species, D_e is related to the diffusion coefficient in water, D_w and the diffusion accessible porosity, ∅, by

$$D_e = \frac{\emptyset}{\tau^2} \cdot D_w \tag{6}$$

where τ is the tortuosity. The effective diffusion coefficient may also be related to the diffusion accessible porosity by an analogue empirical power law formulation of the form

$$D_e = D_w \cdot \emptyset^m \tag{7}$$

where m is an empirical exponent. In natural porous media the power law form of equation (7) is indicative of the fractal geometry of the pore-solid interface. In such a sinuous capillary bundle model the sinuous nature of the bundle reflects the roughness of the pore-solid interface, with fractal properties within some scale limits. The power law form of equation (7) can thus be related to the porosity of a volume element of size l_2, between the lower and upper limits of the fractal region, l_1 and l_2, and to the pore volume fractal D_v, as

$$\emptyset = (l_1/l_2)^{3-D_v} \tag{8}$$

where, for embedded dimensions of three [20], $2 \leqslant D_v \leqslant 3$. The tortuosity of the fractal bundle in a volume element is related to the fractal dimensions of the pore-solid surface, D_s, and pore volume, D_v, as

$$\tau^2 = \emptyset^{2(2-D_S)/(3-D_v)} \tag{9}$$

Substituting equations (7) and (8) into (5) gives

$$D_e = D_w \cdot \emptyset^{1+2(D_s-2)/(3-D_v)} \quad (10)$$

where the fractal dimensions of the pore surface and pore volume can be quantified from (V)SANS analysis as the slope of Q versus I(Q) and r versus f(r) respectively, in the Q-range 10^{-4} Å^{-1} ⩽ Q ⩽ 10^{-2} Å^{-1}.

3. Results

3.1. Petrology

The Carmel Formation comprises shallow marine claystone, siltstone, sandstone, carbonate and evaporite sediments, and forms a regional seal between the Navajo and Entrada aquifers [21]. The Entrada Sandstones contains a number of fine grained siltstone and fine sandstone inter-layers reflecting deposition in sabkha and fluvial wadis [22]. In the Green River drillhole a basal 16 cm-thick claystone to the Carmel Formation acts as a caprock to the CO_2-rich brines in the underlying Navajo sandstone and the inter-reservoir seals within the Entrada Sadstone acts as baffles to the flow of CO_2-charged brines (Figure 1) [10]. The results of quantitative mineralogy, carbonate $\delta^{18}O$ and $\delta^{13}C$ isotopic compositions, and porosity of the sample profiles from the Carmel and Entrada reservoir-seal contacts are presented in Figures 2 and 3.

The primary mineralogy of the Carmel Formation profile comprises illite, quartz, dolomite, K-feldspar, gypsum and hematite, with a significant clay fraction, making this unit a consolidated claystone (Figure 2). The primary mineralogy of the Entrada Sandstone profile is similar comprising illite, quartz, dolomite, K-feldspar and hematite, but with a higher proportion of quartz grains making this unit a consolidated siltstone (Figure 3). The basal sections (7-8 cm) of both profiles are bleached from their original red colour to a pale yellow/grey. These bleached sections are depleted in hematite and Mg-dolomite and enriched in pyrite, Fe-dolomite, illite-smectite and gypsum. SEM and EMPA analysis of the dolomite grains in these sections reveals overgrowths of Fe- dolomite (Figure 4 and 5). The contact between the bleached and unbleached sections shows localized growth of reprecipitated porphyroblast hematite nodules, which are intergrown with covellite (CuS) and chalcopyrite ($CuFeS_2$) (Figure 4). The basal 1-2 cm of each profile are enriched in secondary pore filling illite-smecite, with a distinct platy habit, which tends to form around dissolved and corroded K-feldspar grains (Figure 5). EMPA of this secondary illite reveals a distinct composition from the primary matrix illite (Figure 6). The porosity profile shows a marked increase in porosity just upstream of the hematite dissolution front, but further upstream precipitation of Fe-rich dolomite, pyrite, gypsum and illite-smectite cause a progressive decrease in porosity to values below that of unreacted caprock (Figure 2 & 3).

The observed petrological changes are consistent with a series of interdependent reactions involving CO_2 and H_2S promoting dissolution of hematite following the stoichiometry

$$4Fe_2O_3 + H_2S + 14CO_2 + 6H_2O \rightarrow 8Fe^{2+} + SO_4^{2-} + 14HCO_3^- \quad (11)$$

Dolomite dissolution was coupled with the growth of Fe-dolomite with Fe^{2+} derived from the acid-reductive dissolution of hematite, accompanied by shifts in the O- and C-isotope composition of dolomite cements (Figure 3 & 4). Pyrite precipitated upstream and euhedral hematite, chalcopyrite and covellite precipitated downstream of the hematite dissolution front, with Fe and Cu supplied from primary hematite dissolution, and sulfide from the invading fluid.

Bleaching in the Green River location has previously been related to CO_2-bearing fluids [23-26]. A comparable basal unit from the Carmel Formation from a drill hole free from CO_2 33 km NW of Green River, shows no discernible change in mineralogy or O- and C-isotope ratios as a result of reactions at the base of the caprock [13].

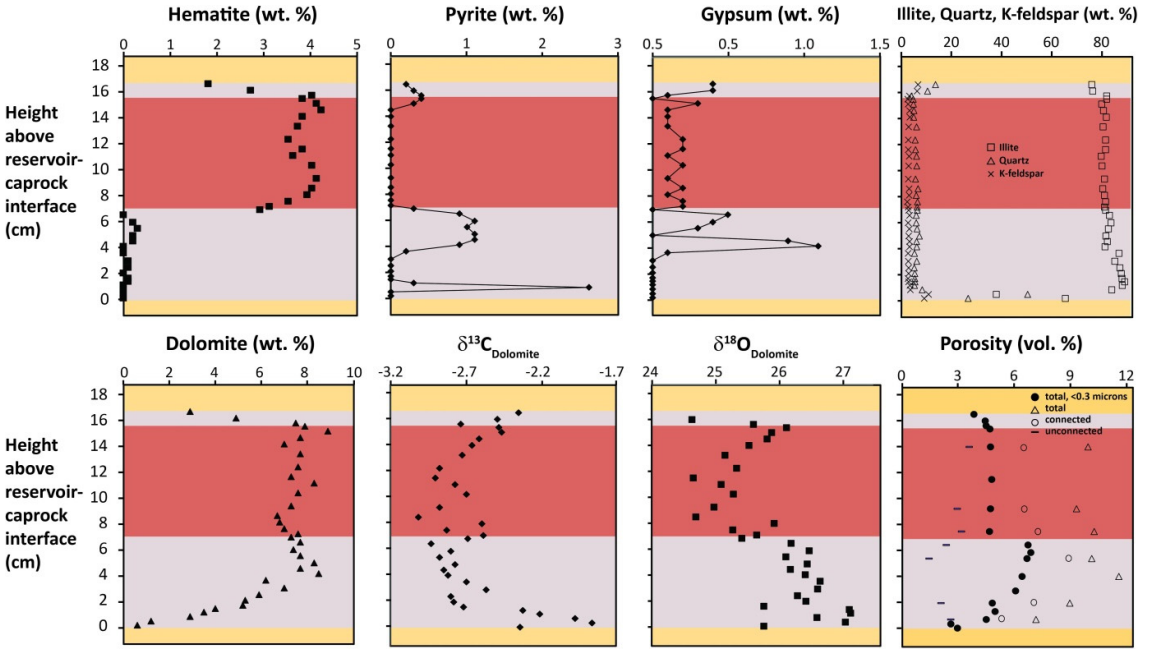

Figure 2 Profiles of XRD mineralogy, carbonate $\delta^{13}C$ and $\delta^{18}O$ and porosity for the Carmel Formation claystone

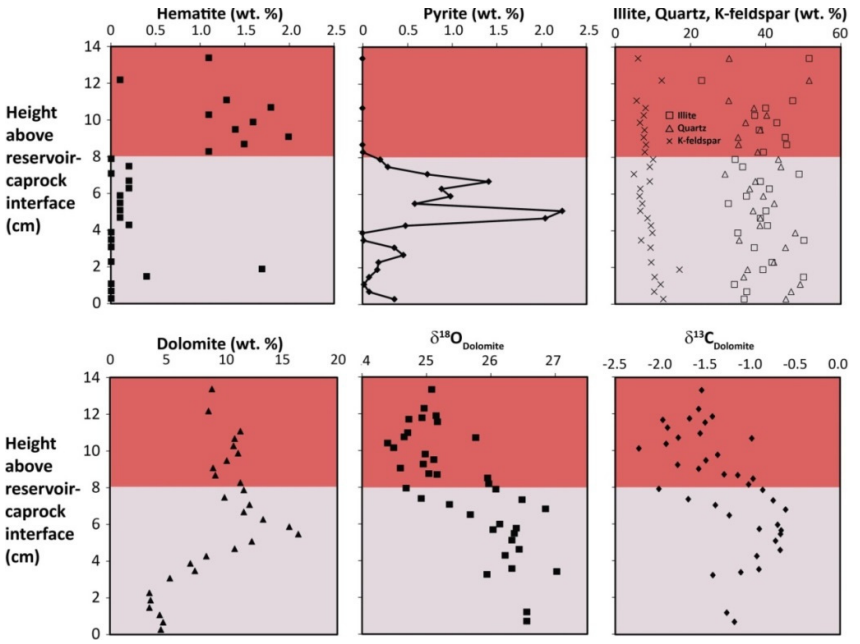

Figure 3 Profiles of XRD mineralogy and carbonate $\delta^{13}C$ and $\delta^{18}O$ for the Entrada Formation siltstone

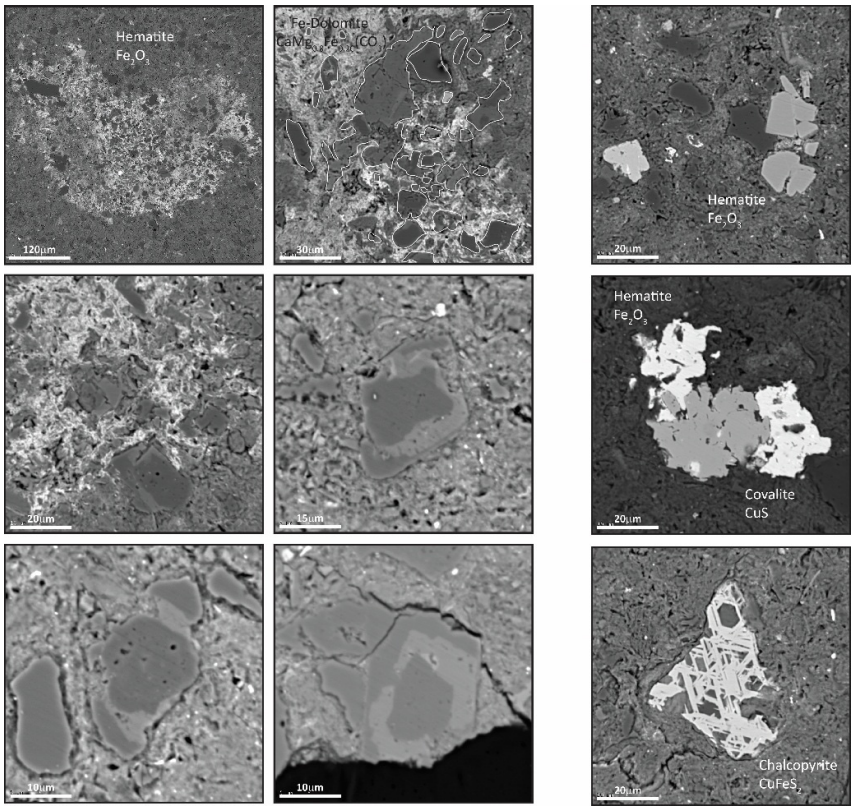

Figure 4 Main panel: SEM images of hematite nodules growing downstream of the hematite dissolution front showing complex intergrowths of hematite and Fe-dolomite. Side panel: Intergrowths of hematite, covellite and chalcopyrite growing upstream of the hematite dissolution front.

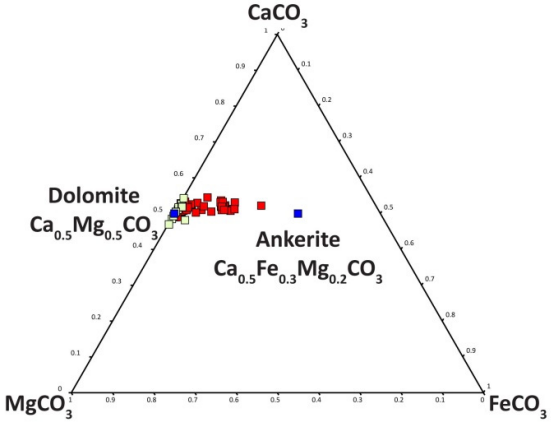

Figure 5 EMPA of dolomite-ankerite compositions in the Carmel claystone. Analyses of dolomite cores are shown as white squares and are close to pure dolomite. Rim analyses are shown as red squares and have vary amounts of ankerite enrichment.

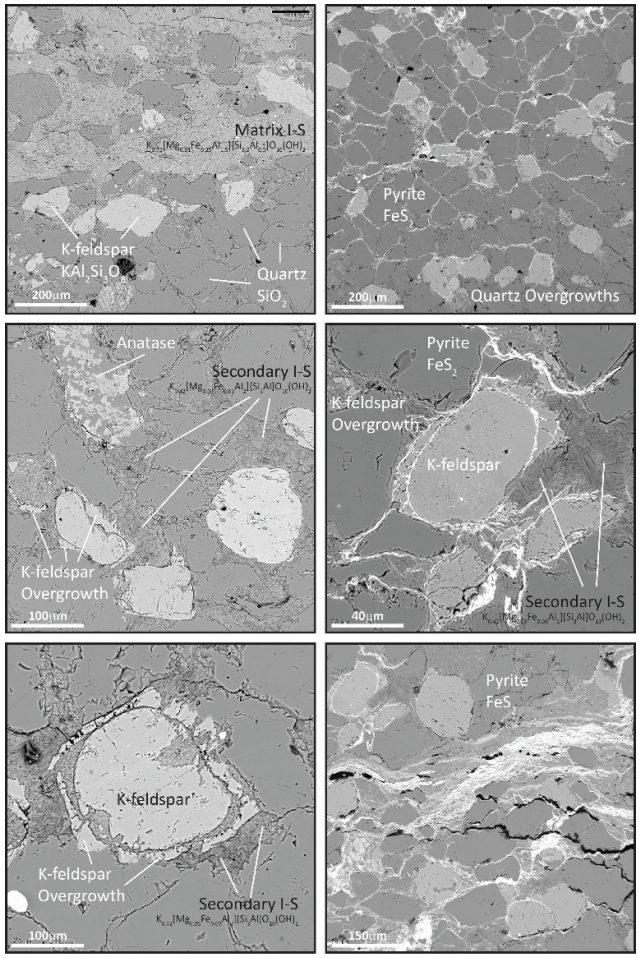

Figure 6 SEM images taken close to the caprock-reservoir interface for the Carmel claystone showing development of secondary porefilling illite after the dissolution of K-feldspar, and the growth of extensive framboidal pyrite

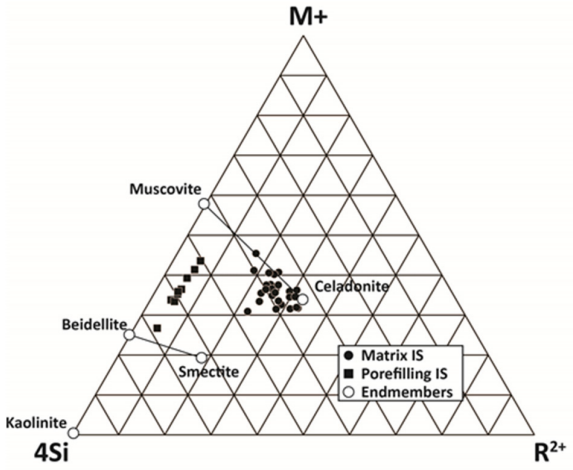

Figure 7 EMPA of illite compositions in the Carmel claystone caprock

3.2. Transport properties

The molecular diffusivities of CO_2 and H_2S in water at 20^0C are ~$2.8x10^{-9}$ $m^2.s^{-1}$ [27]. The calculated porosities, D_s and Dv values imply a τ^2 of ~7.5 and ~3.8 for the Carmel claystone and Entrada siltstone, respectively. This equates to effective diffusivities for CO_2 and H_2S of $1.32x10^{-11}$ $m^2.s^{-1}$ and $2.64x10^{-11}$ $m^2.s^{-1}$ in the unaltered portions of the Carmel and Entrada caprocks, respectively. The calculated diffusivities are at the lower limits of experimentally determined measurements for tortuosity and CO_2 effective diffusivities in shales [27-30] and are consistent with the relative high clay content of these samples. It should be noted that calculation assumes that the porosity is interconnected for pores over the length scales sampled (1.2 to 1500 nm).

4. Modelling Reactive transport in the Caprock

4.1. Analytical Modelling

The mineralogical profiles record the upward diffusion of reactive CO_2 and H_2S bearing fluids into the caprocks. Modelling of the reactive transport enables the timescales over which this alteration has been developed to be examined and an assessment of the impacts that the reactions have had on the caprock porosity evolution. The low permeability of ~ 10^{-21} m^2 of the unreacted caprock implies advective transport must be negligible with Peclet numbers < 10^{-2} [13]. An analytical solution to one-component diffusive transport with mineral dissolution rate described by linear kinetics [31] captures the important physics and informs the essential approximations necessary for reactive transport modelling with multiple components. On initiation of diffusion the reactant mineral volume fraction decreases until the phase is exhausted at the infiltration point. From this time, τ_0 (sec), a reaction front migrates downstream away from the infiltration point, where τ_0 is given by,

$$\tau_0 = \emptyset_S^\infty / \left(V_s k_f \alpha \Delta C_0\right) \tag{12}$$

where k_f (m.sec^{-1}) is mineral reaction rate, α (m^2/m^3) is mineral surface area, Vs is the mineral molar volume ($m^3.mol^{-1}$) and $\emptyset_S^\infty$ is the volume fraction of the reactant mineral phase initially present. $\Delta C_0 = C_{eq} - C_0$ where C_{eq} is the concentration of the component (e.g. CO_2 mol.m^{-3}) in equilibrium with the reactant mineral phase and C_0 is the fluid concentration in the infiltrating fluid, which has been modelled in terms of the moles of CO_2 per mole of hematite in equation 11. The position of the reaction front, l (m) at time t (s) is given by solution of

$$\mathrm{l} + \frac{1}{2}\mathrm{ql}^2 = \frac{1}{q\tau_0}(t - \tau_0) \tag{13}$$

where q (m^{-1}) is given by

$$\mathrm{q} = \sqrt{\frac{k_f \alpha}{D_e}} \tag{14}$$

where D_e is the effective diffusion coefficient defined in equation 10. At $t > \tau_0$ the variation of reactant mineral volume with time and distance (x, m) downstream of the reaction front is given by

$$\emptyset_S(x, l) = \emptyset_S^\infty \left(1 - e^{-q(x-l)}\right) \tag{15}$$

Solutions for the position and velocity of the reaction front (equation 15) are divided into two regimes. If ql>1 (i.e. the Damköhler number $(\mathrm{ql})^2$ is large) reaction rates are fast compared to diffusion rates and the propagation rate depends on the diffusivity of the species driving the reaction and the reaction stoichiometry. For ql<1 the position of the reaction front is a linear function of time and the velocity of the front depends on the reaction rate constant and mineral surface area. Figure 8 illustrates such solutions, calculated for transport of CO_2 in the fluid phase, for time, t, as a function of haematite reaction rate, k_R (mol m^{-2} s^{-1}) given the reaction stoichiometry of equation 11 and

contoured for the effective diffusivity of the caprocks, D_e, estimated from pore volume and fractal pore network modelling of SANS data.

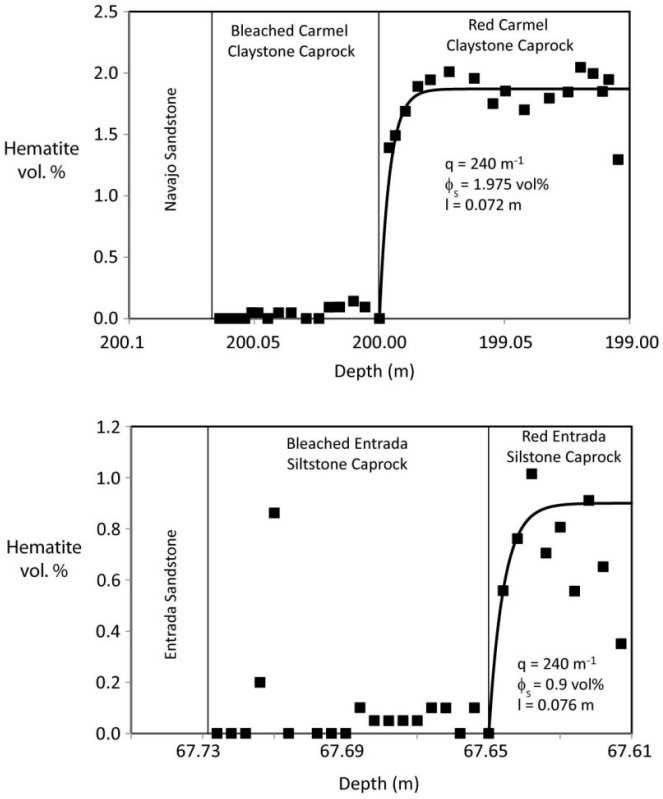

Figure 8 Modelling of hematite mineral modes in the Carmel & Entrada caprock using analytical reactive-diffusion equations

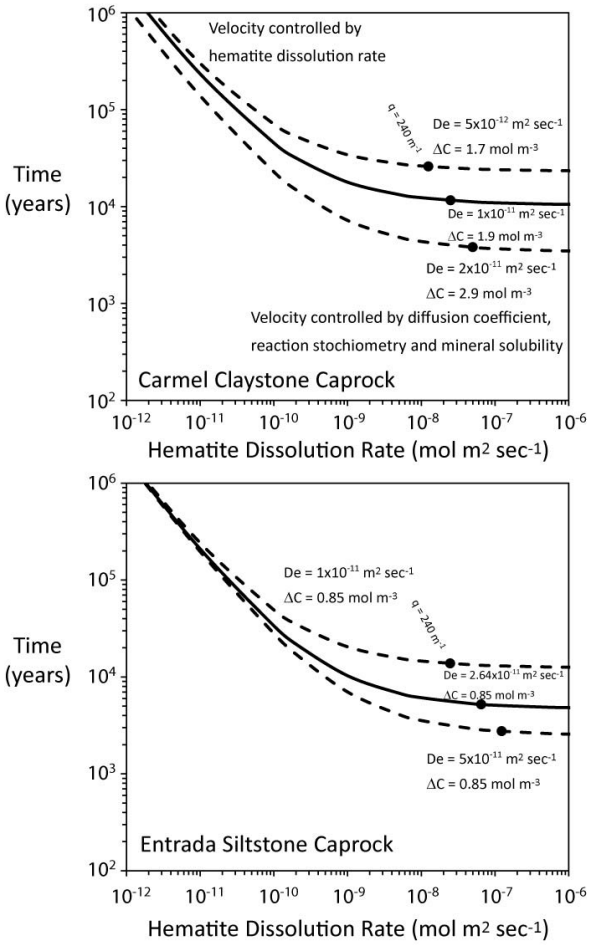

Figure 9 Contours of hematite dissolution rate against time taken for the 7-8 cm Carmel and Entrada caprock hematite dissolution profiles to develop, given uncertainties in the effective diffusivities and mineral solubility

The Carmel hematite mode profile (Figure 2) primarily reflects dissolution described by equation 11, but potentially with additional precipitation of hematite downstream of the reaction front as a result of multicomponent transport. A least-squares best-fit to both profiles gives a value for the exponential constant q in equation 14 of 240 m^{-1} (Figure 8). Given that l = 0.07 m or 0.08 m, ql is > 2 and reaction rates are fast compared with diffusive transport. For De = $1x10^{-11}$ $m^2.sec^{-1}$, the reaction stoichiometry of equation 11 and inlet fluid compositions from downhole sampling [10], these values of q imply a timescale between 3000 and 14,000 years for the Entrada siltstone profile and 4,000 and 26,000 years for the Carmel claystone profile. Hematite dissolution rates estimated from the least-squares best-fit of q are in the range $1x10^{-8}$ to $5x10^{-8}$ $m^2.s^{-1}$. This compares well with laboratory estimates for hematite dissolution rates under acid conditions in the presence of low concentrations of dissolved H_2S [32].

The modelling above only considers transport of Fe_2O_3 and dissolution of hematite as the major component buffering fluid pH and oxidation state. The mineralogical profiles (Figure 2 & 3) show that dissolution/precipitation of dolomite, Fe-dolomite, gypsum, sulphides, K-feldspar, illite and illite-smectite also occurs. The reactive

infiltration was modelled with multiple components and phases by numerical simulation using MoRes-PHREEQC [33], which is a coupling of the geochemical modelling code PHREEQC [34] with Shells in-house reservoir simulator MoRes. A 15cm long 1D reactive-diffusive model comprising 30 cells of 5mm length was constructed of each of the two measured profiles. Each cell initially contained the mineral volumes measured by XRD and porosity measured by (V)SANS in unreacted caprock. The invading pore fluid chemistry was based on analyses of the reservoir fluids [10] with a redox state defined using the SO_4^{2-}/H_2S redox couple. The initial caprock pore fluid chemistry was calculated as that in equilibrium with the caprock mineralogy, with pCO_2, pO_2 and salinity typical of Jurassic marine shales [35]. Models were run assuming local fluid-mineral equilibrium. A D_e value of 5×10^{-11} $m^2.sec^{-1}$ and 2.64×10^{-11} $m^2.sec^{-1}$ was used for all aqueous species for the Carmel and Entrada profiles, respectively. The model timescale was 125,000 years with a time step of 7 days.

The models reproduce the key observations for both profiles (Figure 11). The hematite dissolution front migrates ~ 7-8 cm in $>10^4$ years. Dolomite dissolves downstream of the front and Fe-dolomite is precipitated upstream of the reaction front. Pyrite is precipitated initially close to the caprock-reservoir contact and migrates very slowly. K-feldspar dissolves only at the inlet, driving local precipitation of illite-smectite. The additional complexities observed with multiple zones of pyrite precipitation likely result from the episodic release of CO_2-charged brines by the fault system and are not reproduced with a single pulse model [12, 13].

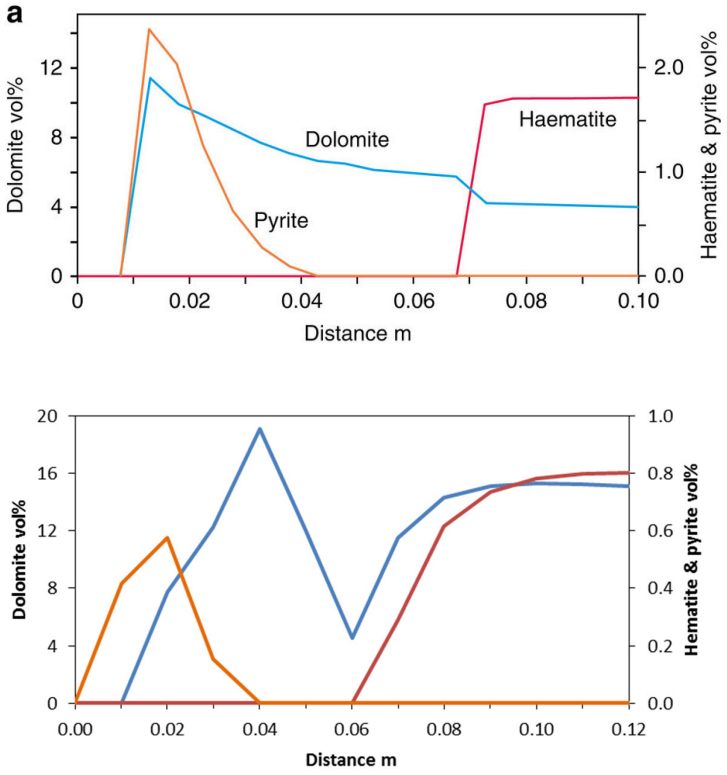

Figure 10 Numerical reactive transport modelling results using MoRes-PHREEQC for a) the Carmel caprock profile and b) the Entrada caprock profile

5. Conclusions

The important conclusion from the analytical and numerical modelling is that the timescale for the development of the 7-8 cm reaction fronts are ~ 1,000's to 100,000 years, consistent with the geological evidence for the duration of the CO_2 supply to the Little Grand Fault system [12]. The propagation of the reaction front is retarded by redox-sensitive mineral dissolution reactions and carbonate precipitation, which reduces the penetration of the mineral alteration into the caprock. Rock buffering reactions are effective at establishing fluid-mineral equilibrium over centimeter length-scales and the reaction progress is controlled by the low transport rates in the caprocks. This study provides evidence for the slow penetration rate of fluid-rock reactions into clay-rich and siltstone caprocks and the development of a stable reaction front without a significant positive feedback loop between porosity enhancement and the velocity of the front. In this caprock CO_2-charged fluid-mineral reactions act to enhance caprock integrity over a time period comparable to than needed for effective geological carbon storage.

Acknowledgements

We thank DOSECC for carrying out the drilling, Morgan Schaller for coordinating activities on the drill site, the core logging team from Utah State University and staff at the Godwin Laboratory, Cambridge for O- and C-isotopic analyses. Funding was provided by NERC to the CRIUS consortium (NE/F004699/1), Shell Global Solutions, the Division of Chemical Sciences, Geosciences, and Biosciences, Office of Basic Energy Sciences, U.S. Department of Energy and DECC who provided a CCS Innovation grant for completion of this work. Data from the BGS is published with the permission of the Executive Director, BGS (NERC). The authors would like to acknowledge Shell for the permission to publish this paper.

References

[1] IPCC (2014) Mitigation of Climate Change. Contribution of Working Group III to the Fifth Assessment Report of the Intergovernmental Panel on Climate Change . ,. Climate Change 2014, eds Edenhofer O, Pichs-Madruga R, Sokona Y, Farahani E, Kadner S, Seyboth K, Adler A, Baum I, Brunner S, Eickemeier P, et al. (Cambridge University Press, Cambridge), p 1435 pp.

[2] Benson SM & Cole DR (2008) CO2 Sequestration in Deep Sedimentary Formations. Elements 4 (5):325-331.

[3] Bildstein O, et al. (2010) Integrative modeling of caprock integrity in the context of CO2 storage: evolution of transport and geochemical properties and impact on performance and safety assessment. Oil & Gas Science and Technology–Revue de l'Institut Français du Pétrole 65(3):485-502.

[4] Busch A & Amann-Hildenbrand A (2013) Predicting capillarity of mudrocks. Marine and Petroleum Geology 45:208-223.

[5] Gherardi F, Xu T, & Pruess K (2007) Numerical modeling of self-limiting and self-enhancing caprock alteration induced by CO2 storage in a depleted gas reservoir. Chemical Geology 244:103-129.

[6] Gaus I, Azaroual M, & Czernichowski-Lauriol I (2005) Reactive transport modelling of the impact of CO2 injection on the clayey cap rock at Sleipner (North Sea). Chemical Geology 217(3-4):319-337.

[7] White A & Brantley S (2003) The effect of time on the weathering of silicate minerals: why do weathering rates differ in the laboratory and field? Chemical Geology 202(3-4):479-506.

[8] Knauss KG, Johnson JW, & Steefel CI (2005) Evaluation of the impact of CO2, co-contaminant gas, aqueous fluid and reservoir rock interactions on the geologic sequestration of CO2. Chemical Geology 217(3-4):339-350.

[9] Kampman N, et al. (2013) Scientific drilling and downhole fluid sampling of a natural CO2 reservoir, Green River, Utah. Scientific Drilling 16:p. 33-43.

[10] Kampman N, et al. (2014) Drilling and sampling a natural CO2 reservoir: Implications for fluid flow and CO2-fluid-rock reactions during CO2 migration through the overburden. Chemical Geology 369:51–82.

[11] Burnside NM, Shipton ZK, Dockrill B, & Ellam RM (2013) Man-made versus natural CO2 leakage: A 400 k.y. history of an analogue for engineered geological storage of CO2. Geology 41(4):471-474.

[12] Kampman N, et al. (2012) Pulses of carbon dioxide emissions from intracrustal faults following climatic warming. Nature Geoscience 5:352-358.

[13] Kampman, N., Busch, A., Bertier, P., Snippe, J., Hangx, S., Pipich, V., Di, Z., Rother, G., Harrington, J.F., Evans, J.P. and Maskell, A., (2016). Observational evidence confirms modelling of the long-term integrity of CO2-reservoir caprocks. Nature Communications, 7.

[14] Shipton ZK, Evans JP, Robeson KR, Forster CB, & Snelgrove S (2002) Structural heterogeneity and permeability in faulted eolian sandstone: Implications for subsurface modeling of faults AAPG Bulletin 86(5):863-883.

[15] Gasparik, M. et al. Geological controls on the methane storage capacity in organic-rich shales. Int. J. Coal Geol. 123, 34–51 (2014).

[16] Ufer, K. et al. Quantitative phase analysis of bentonites by the rietveld method. Clays Clay Minerals 56, 272–282 (2008).

[17] Radlinski AP (2006) Small-Angle Neutron Scattering and the Microstructure of Rocks. Reviews in Mineralogy and Geochemistry 63:363-397.
[18] Hinde A (2004) PRINSAS - a Windows-based computer program for the processing and interpretation of small-angle scattering data tailored to the analysis of sedimentary rocks. Journal of Applied Crystallography 37:1020-1024.
[19] Porod G (1982) General theory. Small-angle X-ray scattering, eds Glatter O & Kratky O (Academic Press, London (UK)), pp 17-51.
[20] Liu J-g, Wang H-t, & Nie Y-f (2004) Fractal model for predicting effective diffusion coefficient of solute in porous media. Advances in Water Science 15:458-462.
[21] Freeman, W. E., & Visher, G. S. (1975). Stratigraphic analysis of the Navajo Sandstone. Journal of Sedimentary Research, 45(3).
[22] Crabaugh, M., & Kocurek, G. (1993). Entrada Sandstone: an example of a wet aeolian system. Geological Society, London, Special Publications, 72(1), 103-126.
[23] Wigley M, Kampman N, Dubacq B, & Bickle M (2012) Fluid-mineral reactions and trace metal mobilisation in an exhumed natural CO2 reservoir, Green River, Utah. Geology 40(6):555-558.
[24] Wigley M, Dubacq B, Kampman N, & Bickle M (2013) Controls of sluggish, CO2-promoted, hematite and K-feldspar dissolution kinetics in sandstones. Earth and Planetary Science Letters 362:76–87.
[25] Wigley, M., Kampman, N., Chapman, H. J., Dubacq, B., & Bickle, M. J. (2013). In situ redeposition of trace metals mobilized by CO2-charged brines. Geochemistry, Geophysics, Geosystems, 14(5), 1321-1332.
[26] Tamimi A, Rinker EB, & Sandall OC (1994) Diffusion coefficients of hydrogen sulfide, carbon dioxide, and nitrous oxide in water over the temperature range 293-368 K. Journal of Chemical Engineering Data 39:330-332.
[27] Amann A, et al. (2011) Sealing rock characteristics under the influence of CO2. Energy Procedia 4:5170–5177.
[28] Berne P, Bachaud P, & M. Fleury M (2010) Diffusion Properties of Carbonated Caprocks from the Paris Basin. Oil & Gas Science and Technology 65(3):473-484.
[29] Wollenweber J, et al. (2009) Caprock and overburden processes in geological CO2 storage: An experimental study on sealing efficiency and mineral alterations. Energy Procedia 1:3469-3476.
[30] Busch A, et al. (2008) Carbon dioxide storage potential of shales. International Journal of Greenhouse Gas Control 2:297-308.
[31] Lichtner PC (1988) The quasi-stationary state approximation to coupled mass transport and fluid rock interaction in a porous medium. Geochimica et Cosmochimica Acta 52:143-165.
[32] dos Santos Afonso M & Stumm W (1992) Reductive dissolution of iron (III)(hydr) oxides by hydrogen sulfide. Langmuir 8: 1671-1675.
[33] Wei, L. (2012). Sequential coupling of geochemical reactions with reservoir simulations for waterflood and EOR studies. SPE Journal, 17(02), 469-484.
[34] Parkhurst DL & Appelo CAJ (2013) Description of input and examples for PHREEQC version 3—A computer program for speciation, batch-reaction, one-dimensional transport, and inverse geochemical calculations: Ch. A43 (USGS).
[35] Turrero MJ, et al. (2006) Pore water chemistry of a Paleogene continental mudrock in Spain and a Jurassic marine mudrock in Switzerland: Sampling methods and geochemical interpretation. Journal of Iberian Geology 32(2):233-258.